Supplemental files

for

Rational Co-Engineering of π-Exciton and Oxygen Vacancy via a Mild Halide-Exchange Strategy: A Sustainable Blueprint for Highly Efficient S-Scheme Photocatalysts

Jingyue Hu[1,2,*], Yuanting Wu[1,*], Weizhi Tian[3], Lihui Guo[1], Xinmeng Zhang[1], Ou Hai[1], Hulin Liu[1], Yunlong Xue[1], Mato Knez[2,4]

[1] *School of Materials Science and Engineering, Shaanxi Key Laboratory of Green Preparation and Functionalization for Inorganic Materials, Shaanxi Laboratory of Advanced Materials, Shaanxi University of Science and Technology, Xi'an 710021, PR China*

[2] *CIC nanoGUNE, Tolosa Hiribidea, 76, 20018 Donostia- San Sebasti´an, Gipuzkoa, Spain*

[3] *School of Mechanical Engineering, Shaanxi University of Technology, Hanzhong, Shaanxi 723001, China*

[4] *Ikerbasque, Basque Foundation for Science, Plaza Euskadi 3, Bilbao E-48009, Spain*

* Corresponding author. E-mail address: bs230211006@sust.edu.cn (Jingyue Hu).

* Corresponding author. E-mail address: wuyuanting@sust.edu.cn (Yuanting Wu).

1. Experimental section

1.1 Preparation of CN Powders

CN powders were synthesized through the thermal calcination of urea under controlled conditions:

Nitrogen-deficient graphitic carbon nitride (CN-1) was synthesized via thermal polycondensation of urea (10 g, 99% purity) in a muffle furnace at 550°C for 4 h under static air (heating rate: 5°C/min).

CN-2: Another batch of 10 g of urea was calcined at the same rate and temperature, but the holding time was reduced to 2 hours.

CN-3: A porous variant of CN powder was prepared by dissolving 5 g of urea in 20 mL of deionized water, followed by ultrasonic treatment for 30 minutes. The dissolved solution was heated at 10 °C/min to 450 °C and held for 1 hour.

1.2 Preparation of BWO Powders

BWO powders were synthesized using a sol-gel method: 0.0018 mol of EDTA and 0.0009 mol of ammonium paratungstate (APT) were dissolved separately in 20 mL of deionized water and stirred for 1 hour until completely dissolved. 0.0012 mol of bismuth nitrate and 0.00005 mol of APT were added to the respective solutions and stirred for 30 minutes. The two solutions were combined and stirred for 1.5 hours. The pH was adjusted to 9–10 using ammonia water, and the mixture was water-bathed at 80 °C for 2 hours to form a transparent gel. The gel was dried at 80 °C for 12 hours to obtain a light-yellow powder. The powder was calcined in two steps: Heated to 350 °C at 5 °C/min and held for 1 hour. Further heated to 750 °C and maintained for 4 hours.

1.3 Preparation of Bi_2SiO_5-Bi_2WO_6 (BSO-BWO) Powders and Halogen solutions

The BSO-BWO composite was prepared via a hydrothermal method. $Bi(NO_3)_3 \cdot 5H_2O$ and $NaSiO_3 \cdot 9H_2O$ were dissolved in deionized water, and ethylene glycol was added to the bismuth solution under stirring. After thorough mixing, sodium silicate solution was added dropwise, followed by the addition of synthesized BWO powder. The mixture was transferred to a PTFE-lined stainless steel autoclave and heated at 180 °C for 12 hours. The final BSO-BWO composite was obtained by washing, centrifugation, and drying.

Halogen solutions were prepared by dissolving specified amounts of NaCl (1.25 mol), NaBr (0.25 mol), or NaI (0.65 mol) in 30 mL of deionized water. The solutions were ultrasonically dispersed for uniform mixing.

1.4 Environmental Sustainability Assessment: Calculation Methods and Details

To quantitatively evaluate the environmental benefits of the proposed synthesis strategy, we conducted an analysis based on three key Green Chemistry metrics: Energy Consumption (Simplified LCA), Atom Economy (AE), and Environmental Factor (E-factor).

1.4.1 Energy Consumption Analysis (Simplified Life Cycle Assessment)

The energy consumption of the "Mild Halide Exchange" strategy was compared with the "Traditional Solid-State Calcination" route commonly used for crystalline bismuth-based photocatalysts. The calculations are based on the specifications of standard laboratory equipment widely used in materials science research.

Traditional Route (High-Temperature Calcination): Equipment Model: Standard Laboratory Box Muffle Furnace (Rated Power: Prated=4.0 kW: P_{rated}=4.0 kW). **Process:** Ramping from room temperature to 550 °C (approx. 1 h) followed by holding for 4 h. **Duty Cycle Assumption:** During the ramping stage, the furnace operates at 100% power. During the holding stage (insulation), the estimated duty cycle is 35% to maintain temperature.

Calculation:

$$E_{trad} = (P_{rated} \times t_{ramp}) + (P_{rated} \times Duty_{hold} \times t_{hold})$$

E_{trad}=(4.0 kW×1 h)+(4.0 kW×0.35×4 h)=4.0+5.6=**9.6** kWh/batch

This Work (Mild Halide Exchange): Equipment Model: Thermostatic Magnetic Stirrer (Heater Power: 0.8 kW; Motor Power: 0.02 kW). **Process:** Reaction at 30 °C for 2 h. **Duty Cycle Assumption:** Since 30 °C is close to ambient room temperature, the heating element operates at a very low duty cycle (estimated at < 5%) to maintain stability.

Calculation:

$$E_{ours} = [(P_{heat} \times \mathrm{Duty}_{heat}) + P_{motor}] \times t_{reaction}$$

E_{ours} = [(0.8 kW×0.05)+0.02 kW]×2 h = (0.04+0.02)×2 = **0.12** kWh/batch

Result: The mild strategy reduces energy consumption by approximately **98.75%**.

1.4.2 Atom Economy (AE) and E-factor

Calculations are based on the stoichiometric reaction: $BiOBr + Cl^- \rightarrow BiOCl + Br^-$.

Atom Economy (AE): Calculated as the ratio of the molecular weight of the desired product (active photocatalyst lattice) to the total mass of reactants involved in the stoichiometric exchange.

Result: **AE** = **86.4%**

Environmental Factor (E-factor): Defined as the mass ratio of waste to the desired product. Since water is used as the sole solvent (which is recyclable) and no organic surfactants or hard templates are employed, the waste consists primarily of washing water and trace exchange salts.

Result: **E**-factor ≈ **0.8**

Table S1. Preparation process parameters of CBB photocatalysts

Sample	BSO-BWO（g）	CN (g)	CN
C_1BB	0.1	0.08	550℃, 4h
C_2BB	0.1	0.08	550℃, 2h
C_3BB	0.1	0.08	550℃, porous

Table S2. Preparation process parameters of CBBX photocatalysts

Samples	CN	V_{NaCl} (mL)	V_{NaBr} (mL)	V_{NaI} (mL)
CBBCl-1	550℃, 4h	5	0	0
CBBBr-1	550℃, 4h	0	5	0
CBBI-1	550℃, 4h	0	0	5
CBBCl-2	550℃, 2h	5	0	0
CBBBr-2	550℃, 2h	0	5	0

CBBI-2	550°C, 2h	0	0	5
CBBCl-3	550°C, porous	5	0	0
CBBBr-3	550°C, porous	0	5	0
CBBI-3	550°C, porous	0	0	5

Table S3. Lattice parameters of the original structure

Structures	a (Å)	b (Å)	c (Å)
BiOCl	7.78679	7.78679	29.9728
BSO	15.1824	5.48120	5.32650
BWO	5.46820	16.5735	5.47500
CN-1	12.3131	7.10940	/

Table S4. Supercell and lattice mismatch rates in heterojunctions

No.	Structures	Supercell	lattice mismatch ratio (%)
C_1BB	BSO	1×3×1	24.94
	BWO	3×1×1	
	CN	1×2×1	
BB - BiOCl	BSO	1×3×1	7.45
	BWO	3×1×1	
	BiOCl	2×2×1	
BiOCl - CN	BiOCl	3×1×1	8.70
	CN	2×1×1	

Table S5. Lattice parameters before and after structural relaxation

Structures	Before structural relaxation		After structural relaxation	
	a (Å)	b (Å)	a (Å)	b (Å)
C_1BB	14.3589	15.3962	16.2130	14.5400

BB - BiOCl	15.7935	16.0735	15.3503	15.9309
BiOCl - CN	23.9933	7.4481	23.8508	7.2059

Table S6. Toxicity and safety profile comparison between the inorganic halogen sources employed in this work and traditional elemental halogen sources

Halogen Source	State (at 25 °C)	Oral LD50 (Rat)a*a*	Hazard Classification (GHS)	Handling Risk
NaCl (Used)	Solid	3,000 mg/kg	Not Hazardous	**Safe**
NaBr (Used)	Solid	3,500 mg/kg	Low Toxicity	**Safe**
NaI (Used)	Solid	4,340 mg/kg	Low Toxicity	**Safe**
***Cl_2* (Gas)**	Gas	N/A (Lethal Gas)	Acute Toxicity, Corrosive	High Risk
***Br_2* (Liquid)**	Fuming Liquid	2,600 mg/kg	Fatal if inhaled, Corrosive	High Risk
***I_2* (Solid)**	Volatile Solid	14,000 mg/kg	Harmful, Irritant	Moderate Risk

a: LD50 (Lethal Dose, 50%) values represent the acute toxicity; higher values indicate lower toxicity. Data obtained from standard Material Safety Data Sheets (MSDS).

The DET calculations for heterojunction systems involving BWO, BSO, BiOCl, and CN-1 reveal insights into their structural and interface properties, which are critical for optimizing photocatalytic performance. As presented in **Table S3**, pristine BWO demonstrates an elongated b-axis (16.5735 Å) due to its layered structure, facilitating electron transport, while CN-1's compact dimensions (a = 12.3131 Å, b = 7.1094 Å) make it highly compatible for heterojunction formation. The lattice mismatch ratios in

heterostructures, as shown in **Table S4**, vary significantly: the C_1BB (CN-BSO-BWO) system exhibits a mismatch ratio of 24.94%, indicating considerable strain at the interface, which could enhance charge separation via interfacial polarization. In contrast, the BiOCl-CN heterojunction displays a lower mismatch ratio of 8.70%, suggesting a more structurally harmonious interface conducive to efficient charge transfer.

Structural relaxation, detailed in **Table S5**, further stabilizes these systems by alleviating interfacial strain. For instance, the a-axis of C_1BB increases from 14.3589 Å to 16.2130 Å post-relaxation, demonstrating significant bond reorganization and improved structural stability. Similarly, the BiOCl-CN system undergoes slight lattice compression, enhancing its structural compatibility. These refined structural parameters amplify the electronic coupling across the heterojunctions, reducing electron-hole recombination and improving photocatalytic efficiency. The synergistic properties of the C_1BB and BiOCl-CN systems underline their potential for solar energy conversion and environmental remediation, with C_1BB showing promise due to its strong interfacial interactions and optimized band alignment.

2. Supplementary Figures

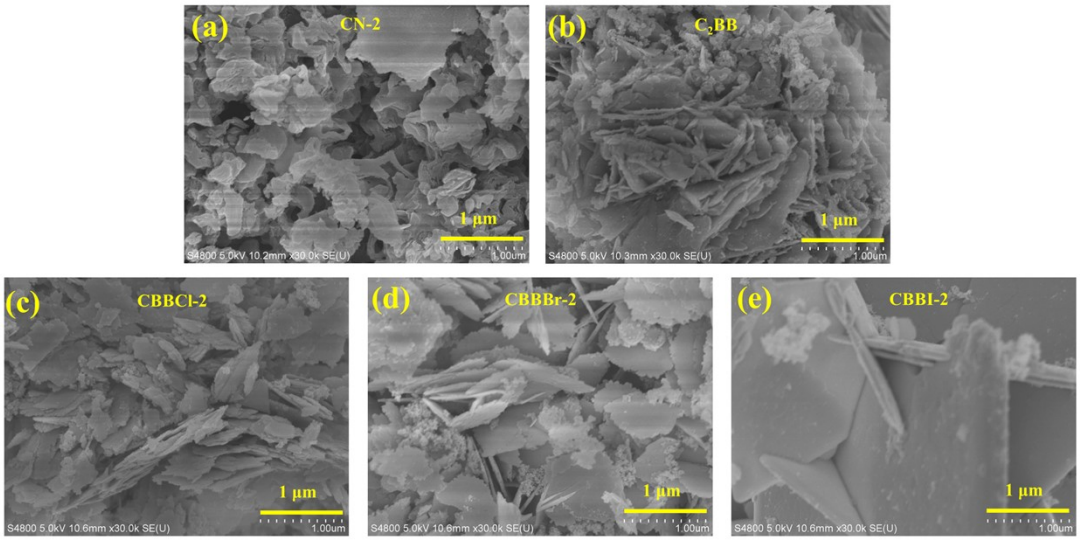

Fig. S1. SEM of photocatalysts: (a) CN-2, (b) C_2BB,

(c) CBBCl-2, (d) CBBBr-2, (e) CBBI-2

The morphological features of photocatalysts prepared via the porous g-C_3N_4 synthetic route (CN-2 series) were examined using SEM **(Figure S1)**. Porous g-C_3N_4 (CN-2, **Figure S1(a))** exhibits an expanded interlayer spacing and more open texture compared to conventional g-C_3N_4 (CN-1), consistent with enhanced surface accessibility resulting from the modified synthesis protocol. The C_2BB composite (**Figure S1(b)**) displays hierarchical structures with increased interparticle voids compared to its C_1BB counterpart.

Upon halogen incorporation, distinctive morphological variations were observed. The chlorine-modified CBBCl-2 composite (**Figure S1(c)**) demonstrates well-interconnected nanosheets with improved spatial organization and dispersion uniformity. In contrast, the bromine-integrated composite (CBBBr-2, **Figure S1(d)**) shows partially irregular assemblies with moderate agglomeration, while the iodine-

modified composite (CBBI-2, **Figure S1(e)**) exhibits pronounced particle coalescence and structural irregularity. These observations parallel the trends observed in the CN-1 series, further confirming chlorine's advantageous role in directing ordered nanostructure formation regardless of the g-C_3N_4 synthesis approach.

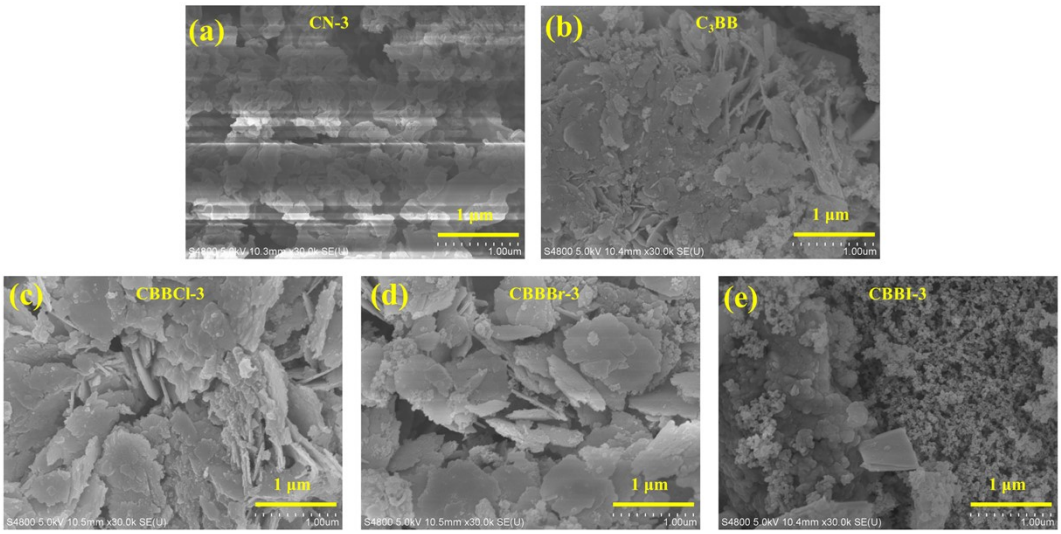

Fig. S2. SEM of photocatalysts: (a) CN-3, (b) CBB-3,

(c) CBBCl-3, (d) CBBBr-3, (e) CBBI-3

The morphological characteristics of photocatalysts prepared via the thermal exfoliation route (CN-3 series) were also investigated (**Figure S2**). Thermally exfoliated g-C_3N_4 (CN-3, **Figure S2(a)**) displays a distinctive stratified architecture with expanded interlayer spacing, resulting from the thermal removal of ammonia and other gaseous species during the exfoliation process. The C_3BB composite (**Figure S2(b)**) exhibits less-defined hierarchical structures compared to both C_1BB and C_2BB counterparts.

The chlorine-integrated CBBCl-3 composite (**Figure S2(c)**) shows partially developed nanosheets with moderate structural regularity, while the bromine-modified composite (CBBBr-3, **Figure S2(d)**) presents irregular assemblies with significant

particle agglomeration. The iodine-incorporated composite (CBBI-3, **Figure S2(e)**) displays the most pronounced structural irregularity and particle coalescence among all three series. These observations indicate that while the thermal exfoliation route produces g-C_3N_4 with enhanced surface exposure, the structural quality of the resulting halogen-integrated heterojunctions is inferior to those prepared via the CN-1 and CN-2 approaches.

Across all three synthetic routes, chlorine integration consistently yields the most well-defined nanostructures with enhanced dispersion and structural uniformity, confirming its superiority for heterojunction construction regardless of the g-C_3N_4 preparation method. These comparative morphological analyses substantiate the selection of the CBBCl-1 composite as the optimal photocatalytic system for further detailed characterization and performance evaluation.

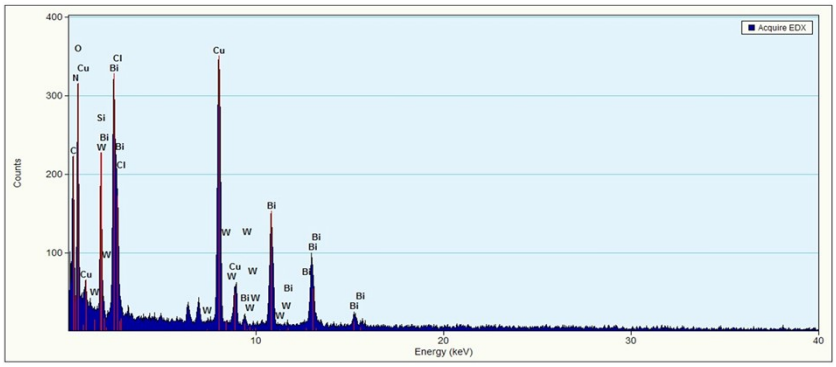

Fig. S3. EDS energy spectra of CBBCl-1 composites

The integration of these phases results in a composite system featuring intricate nanoscale morphologies and heterojunction interfaces, as highlighted in the SEM and HR-TEM images **(Figures 2 and S1**). The multiphase structure is characterized by distinct domains of BSO-BWO and BiOCl intercalated with CN-1, forming highly interconnected nanosheets and nanoflowers. These structural features are pivotal for achieving efficient charge separation and transfer, critical for applications in areas such as photocatalysis and environmental remediation.

The combination of multiple characterization techniques, including XRD, SEM, HR-TEM, and EDS, underscores the complex yet synergistic nature of the composite system. The intricate nanoscale arrangements, combined with the presence of heterojunction interfaces, facilitate enhanced light absorption and charge carrier dynamics. These attributes position the CBBCl-1 composite as a promising candidate for advanced materials applications. The precise control over the multiphase structure and the integration of halides further enhance the material's functionality, paving the way for its potential use in energy conversion and pollutant degradation.

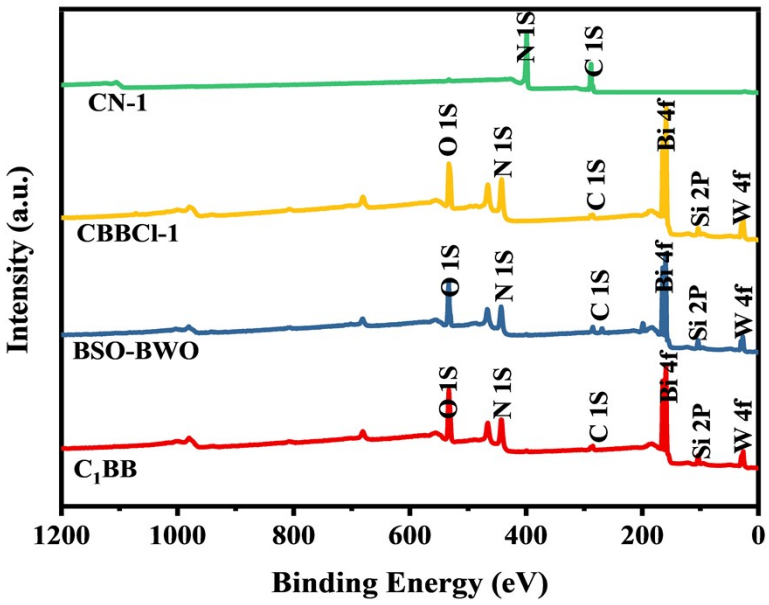

Fig. S4. XPS spectra of Survey

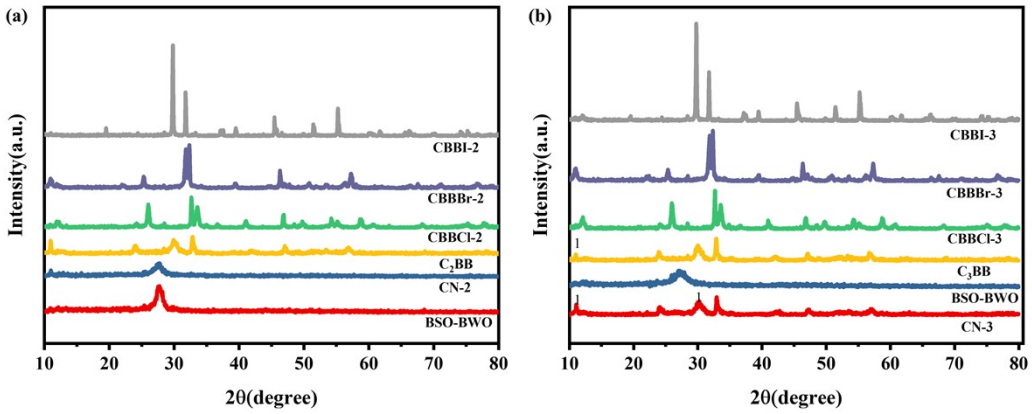

Fig. S5. XRD patterns of (a) (b) different kinds of carbon nitride composite bismuth-based materials

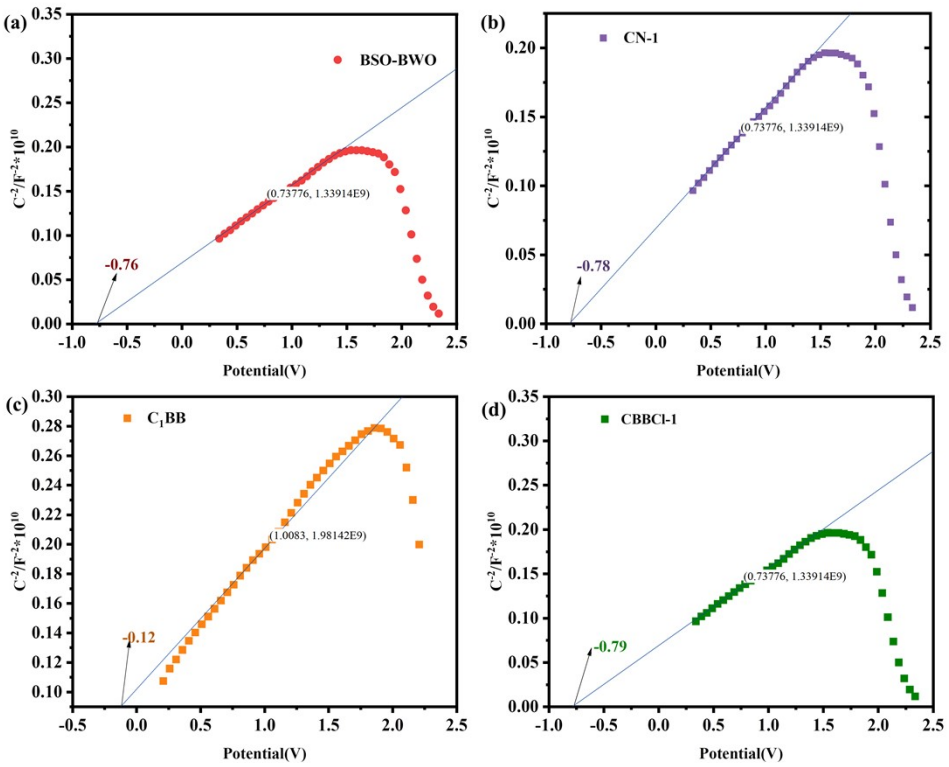

Fig. S6. Mott-Schottky plot for (a)BSO-BWO, (b) C_1N, (c) C_1BB, (d) C_1BBCl

The Mott-Schottky plots provide valuable insights into the electronic properties and flat-band potentials of the materials studied. For **BSO-BWO**, the flat-band potential is approximately **-0.76 V**, confirming its n-type semiconductor nature with electrons as the majority carriers. Similarly, **CN-1** exhibits a flat-band potential of around **-0.78 V**, consistent with its n-type characteristics and photocatalytic properties. When combined into a composite material **C_1BB**, the flat-band potential shifts to approximately **-0.12 V**, indicating enhanced charge transfer and electronic interactions due to the formation of a heterojunction. Furthermore, the introduction of Cl doping in **CBBCl-1** adjusts the flat-band potential to **-0.79 V**, suggesting improved carrier concentration and charge separation, which are beneficial for photocatalytic performance. These results collectively demonstrate the impact of material modifications on the electronic structure and photocatalytic efficiency.

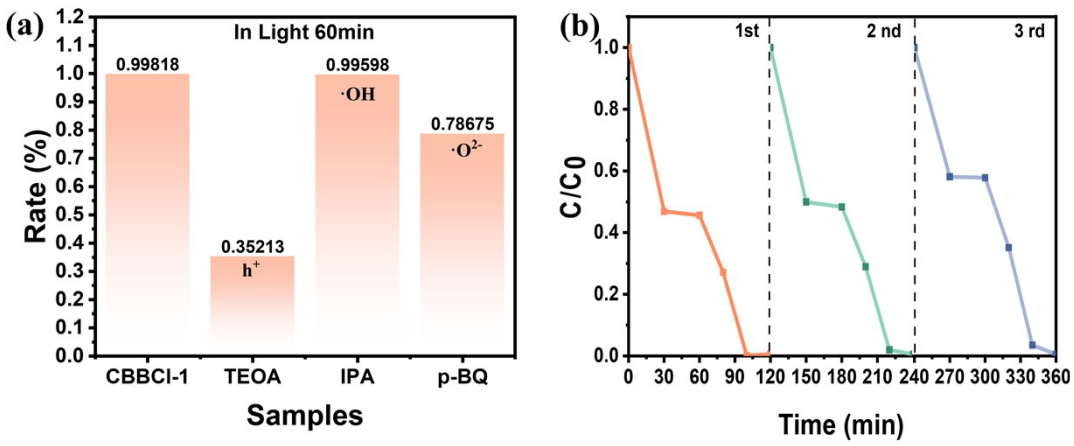

Fig. S7. (a)Capture test plots for CBBCl-1; (b) Experimental performance of CBBCl-1 on cyclic degradation of Rh B at 10 mg/L

To experimentally validate the proposed photocatalytic mechanism and identify the key reactive species, a series of active species trapping experiments were performed, with the results for CBBCl-1 shown in **Fig. S7(a)**. In the control experiment without any scavenger, a high degradation rate was established as the baseline. The introduction of triethanolamine (TEOA), a scavenger for holes (h^+), resulted in a dramatic suppression of the degradation rate to just 35.2% of the original value. Similarly, the addition of p-benzoquinone (p-BQ), a scavenger for superoxide radicals ($•O_2^-$), moderately reduced the rate to 78.7%. In stark contrast, the presence of isopropanol (IPA), an •OH scavenger, had a negligible impact on the reaction, with the rate remaining at 99.6%. These quantitative results provide compelling evidence that photogenerated holes (h^+) are the primary oxidant, with superoxide radicals ($•O_2^-$) playing a significant secondary role. The negligible contribution from •OH is in excellent agreement with the proposed S-scheme charge transfer pathway. Furthermore, the operational stability and reusability of the CBBCl-1 photocatalyst were evaluated through three consecutive cyclic degradation experiments **(Fig. S7(b))**. The catalyst

maintained its high degradation efficiency for all three cycles with no discernible loss of activity, demonstrating its robust structural integrity and excellent stability, which are critical for practical environmental remediation applications.

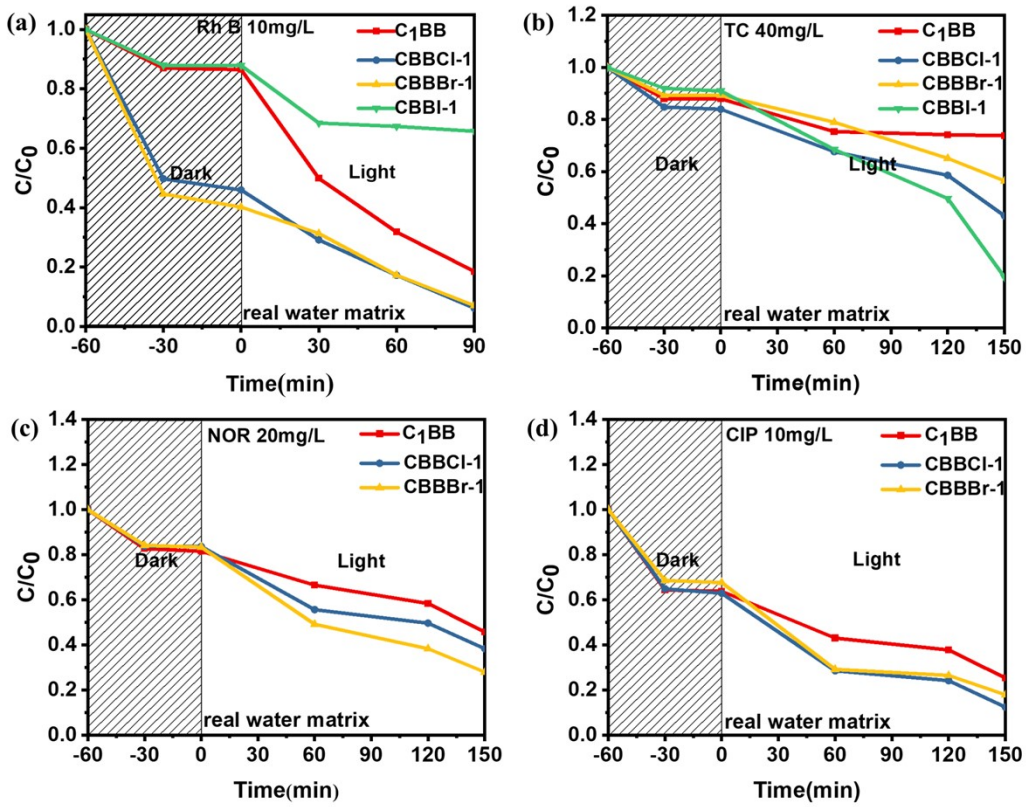

Fig. S8. Photocatalytic degradation profiles in a real water matrix of C_1BB and CBBX for:

(a) 10 mg/L Rh B, (b) 40 mg/L TC, (c) 20 mg/L NOR, (d) 10 mg/L CIP